Propagation of a Realistic Magnetar Jet through a Binary Neutron Star Merger Medium and Implications for Short Gamma-Ray Bursts

Gustavo Soares[1] , Pablo Bosch[2], Davide Lazzati[1] , and Philipp Mösta[2]

[1] Department of Physics, Oregon State University, 301 Weniger Hall, Corvallis, OR 97331, USA; rodrgust@oregonstate.edu

[2] GRAPPA, Anton Pannekoek Institute for Astronomy and Institute of High-Energy Physics, University of Amsterdam, Science Park 904, 1098 XH Amsterdam, The Netherlands

Abstract

The origin of short gamma-ray bursts is associated with outflows powered by the remnant of a binary neutron star merger. This remnant can be either a black hole or a highly magnetized, fast-spinning neutron star, also known as a magnetar. Here we present the results of two relativistic magnetohydrodynamical simulations aimed at investigating the large-scale dynamics and propagation of magnetar collimated outflows through the medium surrounding the remnant. The first simulation evolves a realistic jet by injecting external simulation data, while the second evolves an analytical model jet with similar properties for comparison. We find that both outflows remain collimated and successfully emerge through the static medium surrounding the remnant. However, they fail to attain relativistic velocities and only reach a mean maximum speed of $\sim 0.7c$ for the realistic jet and $\sim 0.6c$ for the analytical jet. We also find that the realistic jet has a much more complex structure. The lack of highly relativistic speeds, which makes these jets unsuitable as short gamma-ray burst sources, is due to numerical limitations and is not general to all possible magnetar outflows. A jet like the one we study, however, could give rise to or augment a blue kilonova component. In addition, it would make the propagation of a relativistic jet easier, should one be launched after the neutron star collapses into a black hole.

Unified Astronomy Thesaurus concepts: Gamma-ray bursts (629); Neutron stars (1108); Relativistic jets (1390); Magnetohydrodynamical simulations (1966)

1. Introduction

The merger of binary neutron stars (BNSs) leads to the formation of another compact object. Its final nature will depend on factors such as the remnant's mass and its ability—or lack thereof—to support itself against its own gravity as it spins down and cools off (see Radice et al. 2020 for a recent review of BNS mergers). The most massive remnants will immediately collapse into a black hole, while the less massive ones will be neutron stars. This latter case may be further subdivided into unstable hypermassive (HMNS) or supramassive neutron stars (Cook et al. 1992, 1994; Baumgarte et al. 2000)—both of which will invariably undergo gravitational collapse into a black hole—and stable neutron stars.

These events are also among the most luminous in the universe (Abbott et al. 2017a). They have been long hypothesized to be the origin of short gamma-ray bursts (sGRBs; Eichler et al. 1989; Narayan et al. 1992) and play a fundamental role in the origin of kilonovae (KN) and the formation of heavy elements; see, e.g., Metzger (2019) for a review.

The prompt gamma-ray emission of GRBs is primarily attributed to two mechanisms. The first of these is internal shocks between shells within relativistic jets powered by the central engine (Narayan et al. 1992; Paczynski & Xu 1994; Rees & Meszaros 1994), while the second is external shocks between the leading shells and the surrounding interstellar medium (Meszaros & Rees 1992; Rees & Meszaros 1992; Katz 1994). Additionally, both mechanisms might be necessary

to explain some observations (Piran & Sari 1998). Nevertheless, in order to power such jets, a compact object such as a black hole or neutron star is required, along with strong magnetic fields.

The multimessenger observation of GW170817 and its electromagnetic counterparts (Abbott et al. 2017a, 2017b) confirmed many of the predictions highlighted above and placed significant constraints on other hypotheses. Yet there still remain a few unanswered questions, in particular regarding the origin and engine powering the associated GRB 170817A, which was first detected 1.7 s after the initial gravitational-wave detection (Abbott et al. 2017a).

Follow-up observations of the KN associated with GW170817 highlighted tensions with simulation results with respect to the amount of KN ejecta and its velocity. Moreover, in order to explain the observations, existing models often require additional constraints related to the neutron star remnant's lifetime, radius, and accretion disk mass (e.g., Bauswein et al. 2013; Hotokezaka et al. 2013; Fahlman & Fernández 2018). Based on this, Metzger et al. (2018) proposed that this tension can be alleviated if the engine powering GRB 170817A is a rapidly spinning, strongly magnetized HMNS remnant with a lifetime of $t \sim 0.1$–1 s.

Multiple groups have explored the feasibility of a magnetar engine for sGRBs, but again, a successful case is highly dependent on factors such as the remnant's lifetime and neutrino effects. For instance, Ruiz et al. (2016) found that a jet was produced only after the HMNS had further collapsed into a black hole, while stable magnetars were hampered by baryon pollution at the polar regions (Ciolfi et al. 2017, 2019; Ciolfi 2020), which in turn prevented the formation of jets and could not be taken care of in the absence of neutrino effects in those simulations.

This approach, where a jet is launched during the HMNS phase, differs from other works, where the jet is launched after the neutron star collapses into a black hole (Nathanail et al. 2020, 2021; Gottlieb et al. 2022b). Other works (e.g., Rezzolla et al. 2011; Kiuchi et al. 2014) capture the entire system evolution from the BNS merger, and the resulting HMNS quickly collapses into a black hole, while Murguia-Berthier et al. (2017, 2021) discussed the features of GRBs triggered by BNS mergers and the jet properties, particularly in the case of GW170817.

Mösta et al. (2020, hereafter M20) performed a series of high-resolution simulations of neutron star merger remnants with a nuclear equation of state and neutrino cooling and heating while adding strong magnetic fields similar to those in magnetars. Due to the high resolution being able to resolve the magnetorotational instability (MRI), M20 found that the strong magnetic fields in the HMNS were capable of launching jets when neutrino effects were included, in particular neutrino cooling, which reduced baryon pollution around the poles and allowed the jets to reach Lorentz factors of 2–5, depending on the simulation details.

Here we evolve the outflowing material from the B15-low simulation from M20, which originated during the HMNS remnant stage, for another order of magnitude in distance and compare those features to those of an analytical jet simulation with similar initial conditions. We find that the outflowing material reaches mean velocities of $\lesssim 0.7c$ in the realistic jet and about $0.6c$ in the analytical jet, although we must consider the numerical limitations affecting this result. The overall structure formed by the ejecta is that of a cocoon, consisting of a shocked jet (which might be relativistic) in the center surrounded by shocked stellar material. Within this cocoon, we found velocities of $\lesssim 0.5c$ in both simulations. Overall, although both jets remained collimated and achieved moderate-to-high velocities, we found that they are most likely unable to power sGRBs. However, this does not necessarily imply that magnetars are, as a whole, unsuitable sources of sGRBs because full neutrino transport has not been included, and the ejected material may be less baryon-rich if neutrino pair annihilation is taken into consideration (Fujibayashi et al. 2017).

In this paper, we describe our simulations in Section 2. The main results are presented in Section 3, and they are further discussed in Section 4. We present our conclusions in Section 5.

2. Simulations: Setup and Overview

We ran two 3D relativistic magnetohydrodynamical simulations with PLUTO 4.4 (Mignone et al. 2007). Our integration setup consists of second-order Runge–Kutta time stepping, an HLLC Riemann solver, and piecewise parabolic reconstruction. We assumed an ideal gas equation of state for the background gas and enforced $\nabla \cdot \mathbf{B} = 0$ through divergence cleaning.

The first of our simulations, which we will refer to as having a "realistic jet," is evolved with periodic injections of outflowing material from a general relativistic MHD simulation of a newly formed magnetar (M20; see Section 2.1 for more details) mapped into our grid, as explained in Section 2.2. The second simulation is described in Section 2.3 and consists of an analytical jet injected at and around the grid inner boundary.

In both cases, we adopt a set of background initial conditions consisting of background gas with ambient density

$\rho_a = 10^{-4} \, \mathrm{g \, cm^{-3}}$ and ambient pressure $p_a = 6 \times 10^{-7} c^2 \, \mathrm{g \, cm^{-3}}$. We also added semispherical material at rest with radially decreasing density and pressure according to a Gaussian profile,

$$\rho(r) = \rho_i \exp(-r^2/2r_*), \qquad (1)$$

where $r_* = 3.8 \times 10^8$ cm, ρ_i is the density of a mass of 2×10^{30} g within a sphere of radius r_*, and $p(r) = 10^{-3}\rho(r)$.

For both of our simulations, we adopted a Cartesian grid extending 8×10^8 cm in the x- and y-directions and 1.4×10^9 cm in the z-direction.

2.1. Input Data

The data mapped into our realistic jet simulation are described in detail in M20. They originated from an ideal GRMHD simulation with an adaptive mesh with the open-source Einstein Toolkit (Schnetter et al. 2004; Löffler et al. 2012; Babiuc-Hamilton et al. 2019) module GRHydro (Mösta et al. 2013). The initial data in that simulation were mapped from a GRHD BNS merger simulation with WhiskyTHC (Radice & Rezzolla 2012) 17 ms after the BNS merger. The details of this mapping can be seen in M20, but in summary, the mapping occurred at $t_{\mathrm{map}} - t_{\mathrm{merger}} = 17$ ms, with a magnetic field given by $A_r = A_\theta = 0$; $A_\phi = B_0 r_0^3 (r^3 + r_0^3)^{-1} r \sin\theta$, where $r_0 = 20$ km and $B_0 = 10^{15}$ G, and an outer boundary of ~ 355 km.

The simulation in M20 employs the equation of state of Lattimer & Douglas Swesty (1991), with $K_0 = 220$ MeV, along with the neutrino leakage and heating approximations of O'Connor & Ott (2010) and Ott et al. (2012). It tracks electron neutrinos, electron antineutrinos, and heavy-lepton neutrinos, the latter being treated as a single species. Neutrino cooling is implemented by approximating energy-averaged neutrino optical depths followed by local estimates of energy and lepton loss rates, while neutrino heating is approximated using a prescription for the neutrino heating rate. It depends on the neutrino luminosity as predicted by the neutrino leakage approximation along radial rays, as well as the electron mass, neutron mass, speed of light, rest mass density, neutron (proton) mass fraction for electron neutrinos (antineutrinos), mean squared energy of the neutrinos, and mean inverse flux factor. The explicit prescription and details can be found in M20. Finally, the mapped GRHD BNS remnant is endowed with an ad hoc parameterized magnetic field prescribed through the vector potential with $A_r = A_\theta = 0$ and $A_\phi = B_0 r_0^{03}(r_0^{03} + r^3)^{-1} r \sin\theta$. The parameters B_0 and r_0 control the overall strength and the falloff of the magnetic field, respectively. In M20, the numerical evolution was carried out at three different resolutions with values $B_0 = 10^{15}$ G to have magnetar-level magnetic field strengths and $r_0 = 20$ km to keep the magnetic field nearly constant within the HMNS. Additionally, to prevent violations of the divergence-free constraint of the magnetic field, $\nabla \cdot \mathbf{B} = 0$, a constrained transport scheme is employed. In this work, we map the first level of the lowest-resolution simulation, B15-low, from M20 onto our grid as described in Section 2.2.

2.2. Data Injection

Our Cartesian grid for this simulation was constructed as follows. We kept a $237 \times 237 \times 237$ box at the origin of our simulation, in which the jet was injected. This corresponds to a cube of ~ 420 km in each direction. This was chosen to match the 237 cells in the xy-plane in the original simulation (within their first level of adaptive mesh refinement (AMR)) and

preserve the original jet as best as possible without too many interpolations into grids with drastically different sizes, which could lead to inaccuracies in the data as they were injected. Within this box, all of the cells have the same size as in the original simulation within one level of AMR, with a resolution of $h = 1.77$ km. We then proceeded to logarithmically extend this original box along the x- and y-directions with 100 cells on either side. Finally, we extended the z-direction by adding 600 cells in a logarithmic grid. In total, our grid has 437 cells in the x- and y-directions and 837 cells in the z-direction.

The snapshots are extracted from M20 at 0.15 ms intervals during the (quasi) steady-state operation of the jet, which lasts about 5 ms. For reference, in M20, the HMNS is evolved roughly 23 ms before collapsing to a black hole. In our current simulation, we inject these snapshots at the same rate as they were extracted, 0.15 ms, keeping the time interval fixed. Once all of the snapshots are injected, we restart the procedure until the end of the simulation, effectively cycling over the available snapshots and treating the injection process as a loop. Given that we are looping over the (quasi) steady-state operation of the M20 simulations, this scheme provides a reasonable approximation for a long-lived jet. The total evolution time is ~ 67 ms (i.e., around 13 completed injection cycles); thus, any specific features arising from jet launching or the eventual collapse of the HMNS will not be reproduced here. Carrying out this simulation on a big domain for a relatively long time without reducing the dimensionality was made possible by the simplification of the equation of state and by being away from the compact object, allowing us not to be concerned about resolving it. This allowed us to use a more efficient special relativistic code and significantly increase the time step. A similar technique was used by Lazzati et al. (2021) and Pavan et al. (2021). In those works, however, an analytic jet was injected into a realistic ambient medium, while here we attempt the opposite feat by injecting a realistic jet into an analytic environment.

Figure 1 shows a few physical quantities of interest—both background and injected—in the equatorial plane for $z = 0$ at the start of the simulation ($t = 0$ s). The four panels show (a) the gas density ρ, (b) the gas pressure p, (c) the velocity v_z along the z-direction, and (d) the plasma β. The central material corresponds to the data mapped from M20 into our grid. Data mapping occurred within a circle of radius 0.21×10^8 cm; this length was chosen because it corresponds to the first level of grid refinement in M20. Decreasing radially in the xy-plane are the extra density and pressure representing stellar material. Along the positive x- and y-directions as we transition from the injection region toward the rest of the simulation domain, there are two small bulging features in all panels. These are numerical in nature and likely occurred during data interpolation. They do not seem to affect the evolution of our simulation.

Looking at the panels in Figure 1, we can also note a hollow geometry in the jet. Its central axis is characterized by lower densities compared to the rest of the material as we move away from this axis (evidently discarding the low-density region outside of the injection area). This lower density along the jet's axis is accompanied by higher pressure—which remains relatively constant within the injected area—and low β, an indication of high magnetization.
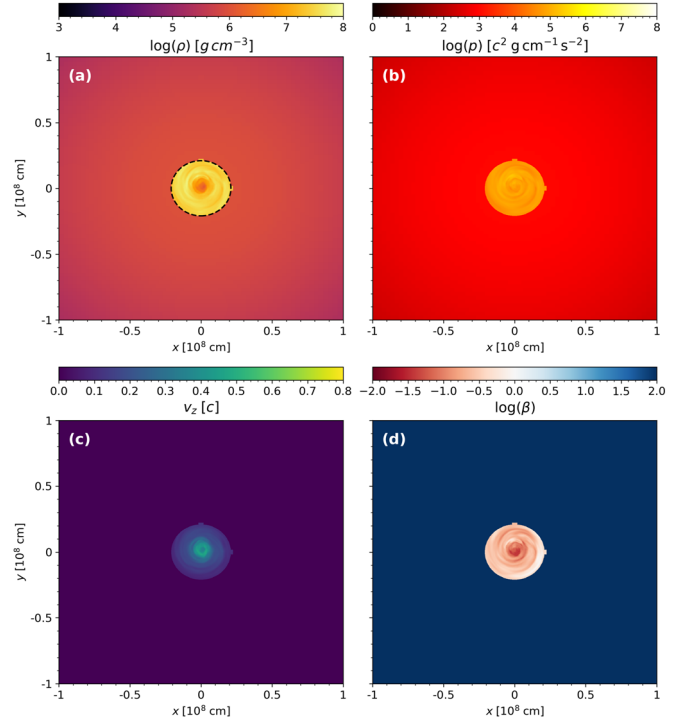

Figure 1. The xy-plane cut at $t = 0$ s of the following quantities: (a) gas density ρ, (b) pressure p, (c) velocity v_z along the z-direction, and (d) plasma β, all at $z = 0$ at the beginning of the realistic jet simulation, zoomed in to focus on the material mapped from M20. Injection occurred within a radius of 0.21×10^8 cm from the xy-plane origin; this region is shown in panel (a) as a black dashed circle.

2.3. Analytical Jet

The background initial conditions used in this simulation are the same as those used in the realistic jet simulation. Our grid for this simulation differs slightly from that; here we have a total of 440 cells in the x- and y-directions, with 200 of these concentrated within a radius r_0 in the xy-plane, taken to be the initial radius of the domain in which we injected our data in the previous simulation. Finally, there are 600 cells in the z-direction. Our prescription for the jet closely follows that of Mignone et al. (2009, 2013) and Gottlieb et al. (2020), with a few modifications aimed at matching as much as possible the values of quantities in this simulation to those of our data-injected simulation. Within r_0, we assume a density ρ_0, which is taken to be the mean density in the injection domain of M20 and is then radially smoothed out as we multiply the density along the xy-plane by the profile

$$\frac{1}{\cosh(r/a)^8}, \tag{2}$$

where $a = r_0/2$ and $r = \sqrt{x^2 + y^2}$. Within the jet, the purely toroidal magnetic field is given by $B_\phi(r) = \gamma b_\phi(r)$, where

$$b_\phi = \begin{cases} b_m r/a, & \text{if } r \leqslant a \\ b_m a/r, & \text{if } a < r < r_0, \end{cases} \tag{3}$$

and $b_m = \sqrt{-4 p_0 \sigma_\phi / [a^2 (2\sigma_\phi - 1 + 4 \log a)]}$. Here $\sigma_\phi = 1$ is the toroidal magnetization parameter, and p_0 was taken from the data-injected simulation, being the mean pressure within the injected domain, $p_0 = 7 \times 10^{-5} c^2$ g cm^{-3}. Finally, the pressure

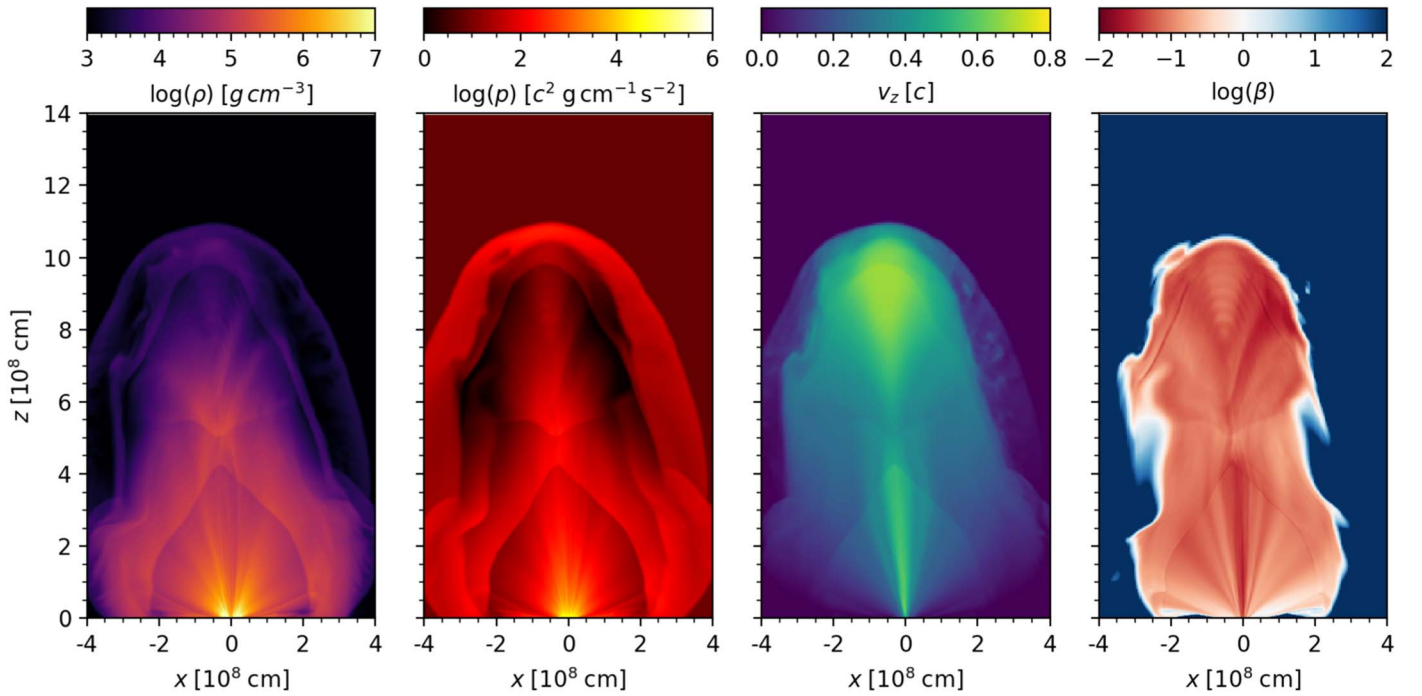**Figure 2.** Meridional slice, *xz*-plane, of the density ρ, pressure p, velocity in the *z*-direction v_z, and plasma β (left to right) in the realistic jet at a late time in the simulation.

inside the jet, p_j, is given by

$$p_j(r) = p_0 + b_m^2[1 - \min(r^2/a^2, 1)], \quad (4)$$

which is also multiplied by Equation (2). The jet's initial velocity is $v_j \sim 0.4c$.

3. Results

3.1. Realistic Jet

The four panels in Figure 2 display, left to right, the gas density, pressure, velocity in the *z*-direction, and ratio between gas and magnetic pressure $\beta = p_g/p_m$. This was taken at a late stage in our simulation.

The first two panels, showing the gas density and pressure, do not present clear, collimated outflows, although this is clearly seen in the velocity panel, where the central part of the outflows is moving with higher velocities ($\sim 0.7c$) compared to its surroundings. Furthermore, the plasma β suggests a complex magnetic structure, which we discuss in Section 4.2.

One noticeable aspect of the jet in this simulation, which can be clearly seen in Figure 2, is that it gets pinched roughly between $z \sim 4 \times 10^8$ and 5.5×10^8 cm, where the presence of two shocks is clearly visible. These shocks appear much earlier on, as the outflows first start interacting with the surrounding material, and propagate as the simulation evolves. There, pressure and density both increase upon the bottom shock, while velocity decreases. In the top shock, around $z \sim 5.5 \times 10^8$ cm, this behavior is reversed; density and pressure start to decrease, while the mean velocity starts to increase again. We also notice, near the head of the jet, the presence of further shocks associated with the interaction between the jet, the surrounding material, and the external medium. This is characterized by a sudden increase in both pressure and density, while the velocity slowly decreases downstream.

It should be noted that the jet in this simulation tilts a bit toward the left side in the *x*-direction (and also a little toward the right in the *y*-direction). Although this behavior is fairly normal in jets (Mignone et al. 2013), we cannot elaborate much on its future behavior; i.e., we cannot say whether this tilt would be reversed or become even more pronounced. This is due to the very nature of our injection process, which consisted of 38 snapshots being mapped into our grid in a constant loop. Hence, if the tilt was already forming as the snapshots were being injected, it is unlikely that its behavior would have changed in the spatial domain covered by this simulation. Evolving the jet for longer periods and distances could possibly lead to a further change in the jet behavior. Similarly, the injection of more data could also lead to a different behavior. Still, kink instabilities could lead to magnetic reconnection sites within the jet and subsequent particle acceleration along current sheets.

3.2. Analytical Jet

The analytical jet shows a qualitatively similar behavior in many aspects when compared to the realistic jet. As seen in Figure 3, which is analogous to Figure 2, the presence of a shock is visible around 8×10^8 cm, although this is a very symmetric shock, with an X-shaped propagation, and the jet retains its overall form for the entire duration of the simulation; i.e., we found no significant pinching occurring along the jet. Having said this, we do notice a decrease in density and pressure along with an increase in velocity at $z \sim 8.2 \times 10^8$ cm, which is similar to the behavior of the realistic jet.

As suggested by the plasma β, the analytical jet appears to be far more collimated than the realistic jet. This could be due to our choice of the toroidal magnetization parameter σ_ϕ, which was initialized at $\sigma_\phi = 1$. Overall, the jet retains a nearly axisymmetrical structure throughout the entire simulation, and we found no signs pointing toward a change in that structure.
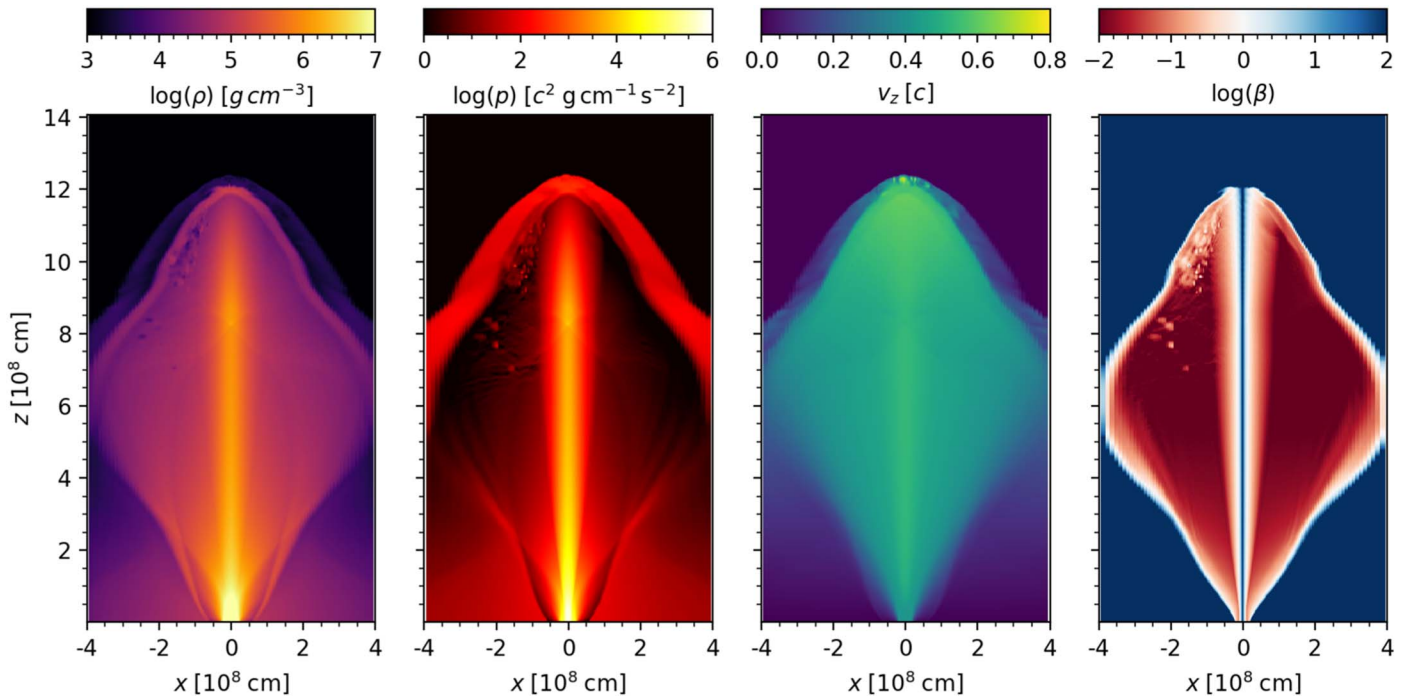
Figure 3. Meridional slice, *xz*-plane, of the density ρ, pressure *p*, velocity in the *z*-direction v_z, and plasma β (left to right) at a late time in the simulation for the analytical jet initial data.

Furthermore, compared to the realistic jet, we see that the central axis of the analytical jet has a very clear high-β region. Although the magnetic fields are comparable in both simulations, there is a striking difference in the pressure, as can be seen in the second panel of Figures 2 and 3, which accounts for this difference.

4. Discussion

4.1. Jet Velocities and sGRBs

The similarities in density and pressure between the two simulations are not unexpected, considering that our analytical jet had its initial values for these quantities chosen so that they would be similar to those in the realistic jet simulation. In order to better track and visualize these features, we traced the profiles of a few quantities, namely, the density, pressure, and velocity, along the jet. We did this by locating the jet axis—taking into account its tilt—and then taking the mean values of these quantities within a certain distance of the jet's central axis. This distance was obtained as follows. We first determined the jet axis by looking at the points on both the *xz*- and *yz*-planes where β was lowest and v_z was highest. We then determined, for each point on the axis, a circle along a plane perpendicular to it to account for the jet being tilted. The circle radius is $\sim 10^7$ cm and was chosen by looking at the profiles for those quantities along cuts through these planes. This process was simplified for the analytical jet, as we did not have to deal with a tilted jet. The profiles are shown in Figure 4. Top to bottom, they are the mean density, pressure, and velocity along the portion of the outflows described above.

The features that we have qualitatively discussed before are better seen here. The shocks in the realistic jet do not appear to be very well defined in Figure 4, but this is simply because the shocks in this jet are "pointy" (see Figure 2), marking the boundary between shocked and unshocked jets, and taking the

average values of quantities within a small distance from the jet axis makes the shocks appear less obvious in Figure 4.

The appearance of GRBs is associated with multiple factors. Crucial, though, are the high speeds in the jet, while moderate-to-high speeds in the cocoon could also lead to sGRBs (Gottlieb et al. 2018). Since our engine powering the realistic jet is a neutron star before its collapse into a black hole, there are a few additional factors that affect the jet's properties that were taken into account in M20. For instance, neutrino cooling reduces baryon pollution in the polar regions, which in turn allows for the launch of faster jets. However, the main question still remains whether the jets are fast enough.

The velocities shown in Figure 4 are mean values within a small radius from the jet's central axis. We see that the jet reaches mean velocities of up to $\sim 0.71c$ in the realistic jet simulation and $\lesssim 0.6c$ in the analytical jet. These correspond to Lorentz factors of $\Gamma \lesssim 1.45$; i.e., both jets only achieve moderate velocities, which suggests that they are unsuitable as sGRB sources.

We note that, in M20, Lorentz factors of ~ 2 were found in the jet. Still, it is possible that those speeds were not maintained up to the moment of injection into our simulation, and the difference between those Lorentz factors and the ones we have here are not significant. Moreover, we can also estimate the Lorentz factor that could be achieved by our jet by using $\Gamma_{\mathrm{max}} = \Gamma_{\mathrm{inj}}(1 + 4p/\rho + \sigma)$. Our values of ρ, p (see, for example, Figure 4), or β (Figure 1) do not suggest that such an increase would be substantial. Even if all magnetic energy could be used to power the jet, we would still obtain $\Gamma_{\mathrm{max}} < 5$ for the values of Γ, density, and pressure encountered along the jet.

This can be seen in Figure 5, which shows that the magnetization σ does not reach high values in either jet. That said, we must factor in the effects of numerical constraints in our simulations. The simulation box in M20 was small, which
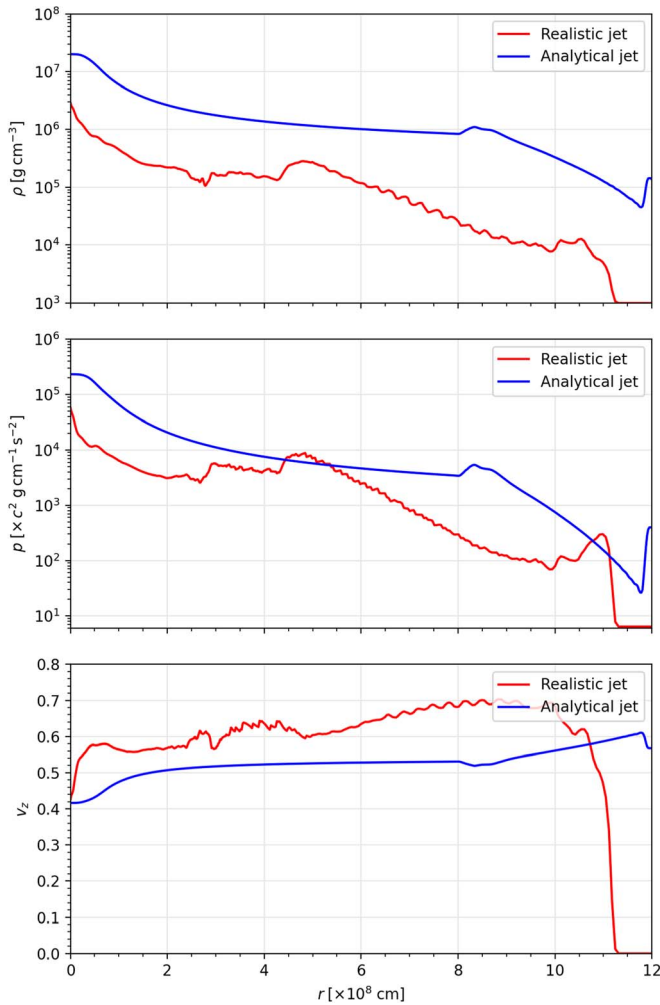
Figure 4. Profiles of the mean values of the density (top), pressure (middle), and velocity (bottom) within 3.5×10^7 cm of the jet axis for the realistic (red) and analytical (blue) jets at a late stage.

Figure 5. Meridional slice, xz-plane, of the magnetization σ along the jet imported from M20 (left) and the analytical jet (right).

in part motivated our decision to propagate their jet further, and even in this work, we cannot extend it much beyond 10^9 cm. This is due to both computational limitations and the fact that we did not want to extend the looped injection of the M20 jet into our grid, as the HMNS has already collapsed by the time our simulation ends, and we cannot account for further changes in the jet that would occur once the black hole is formed.

If such constraints are not present, we can argue that any limitations would now be related to the physics associated with the jets. Since we are propagating an already existing jet, it is reasonable to expect that any significant changes would have to be introduced at the early stages of a simulation, i.e., something analogous to M20. If a long-lived jet would be able to maintain its hollow nature, with comparatively low density and high pressure within its central axis, it could achieve higher Lorentz factors and therefore be a viable source of sGRBs. Furthermore, the analytical jet is limited by the way the initial quantities are prescribed, which is not the same as in the realistic jet. Even though both jets evolve differently, the initial velocity conditions are not conducive to reaching high Lorentz factors. Further propagation over at least another order of magnitude in distance where the background density drops significantly could, however, clarify the behavior of the jet and, in particular, its terminal speed.
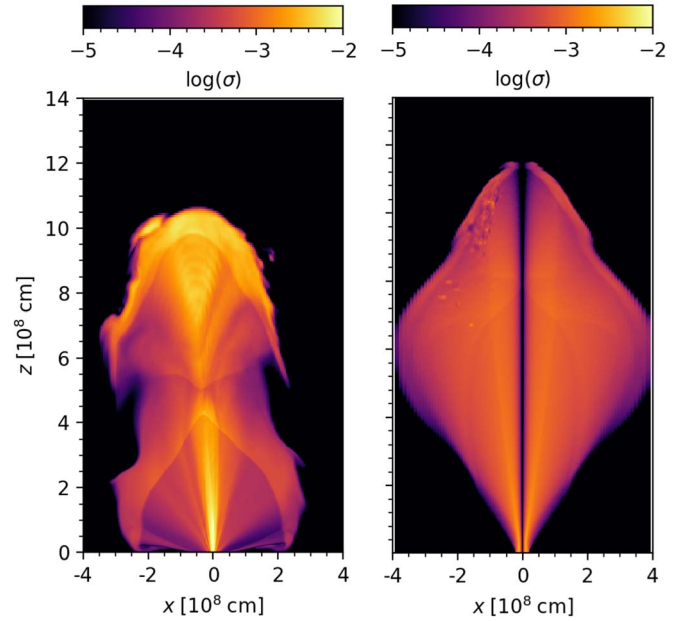
With a hybrid approach, Pavan et al. (2021) evolved a top-hat jet within a realistic BNS merger background, similar to Lazzati et al. (2021), and showed that the jet achieves a terminal Lorentz factor of ~ 40. Furthermore, Gottlieb et al. (2022a) showed that a self-consistent jet launched upon a collapsar reached Lorentz factors of $\lesssim 30$ at distances of 10^{12} cm; comparatively, they propagated the jet 3 orders of magnitude more than in our evolution. Lazzati et al. (2021) also carried out a comparison with a fully analytical setup, like we have done in this work. Their findings are analogous to ours. The realistic and analytical simulations show comparable evolution but differ in some important details. In both cases, the realistic setup shows a less smooth jet, characterized by the presence of small structures in its velocity, density, pressure, and—in our case—magnetization.

Gottlieb et al. (2018) presented a model in which a cocoon shock breakout could power GRB 170817A, provided the material in the cocoon achieved moderate-to-high velocities, $v \gtrsim 0.6$–$0.8c$. The total ejected mass in M20 is around $1.1 \times 10^{-3} M_\odot$, and with the exception of the jet, none of the ejecta achieved velocities above $0.5c$. Upon propagating that jet, we found that the cocoon material still falls short of achieving velocities above $0.5c$. We found the same for the analytical jet. This further suggests that neither jet studied here is likely to lead to sGRBs in this scenario. However, the scenario proposed by Gottlieb et al. (2018) requires a tail of high-velocity ejecta with a characteristic speed of ~ 0.6–$0.8c$. While such a component could be dynamical in origin, it is also possible that it is provided during the metastable neutron star phase of the remnant. Our simulations show that, indeed, a collimated outflow with the required characteristics is produced by a magnetar jet.

The approximate neutrino leakage scheme, employed in M20, captures the overall neutrino energetics up to a factor of a few when compared to a full transport scheme in core-collapse supernova simulations. The dependence on the energy, the deposition of momentum, and neutrino pair annihilation are

not included and are possibly important in the jet formation process and the outflow properties. The approximate neutrino leakage scheme used in M20 thus introduces some uncertainties and can be a potential source of errors.

It should be noted that the analytical simulation makes no direct assumptions regarding factors such as the neutron star equation of state, neutrino effects, or baryon pollution, all of which contribute to the neutron star lifetime, jet launching capabilities, and jet velocity. Yet the fact that both jets attained similar moderate velocities suggests that simply assuming a low/moderate initial velocity for the jet in the analytical simulation—which in a realistic case would be due to the aforementioned factors—partially makes up for the lack of explicit neutrino effects in this simulation. Nonetheless, the lack of relativistic speeds along the jets or moderate-to-high speeds in the cocoon makes them unlikely to produce sGRBs.

Even though the jet we study in this work does not move fast enough to power an sGRB jet, we notice that it remains collimated and reaches its terminal velocity, accelerating to its full potential. This makes it very interesting to explore, in a future follow-up work, a magnetar jet with higher acceleration potential, for example, due to higher magnetization or lower baryon loading.

4.2. Magnetic Field Structure

The plots of β in Figures 2 and 3 suggest a very noticeable difference in the magnetic field structure of the two jets that we evolved. At first, this is somewhat expected, given the circumstances in which both simulations were started; the realistic jet is an evolution of data that had already been subjected to previous magnetic field evolution, while the analytical jet was injected with a magnetic field profile given by Equation (3).

We show in Figure 6 a contour plot of the z-component of the jet velocity along with the magnetic field lines. In M20, the purely poloidal magnetic field initial configuration develops a strong toroidal component during the evolution. The field lines in this case retain their helical configuration even after propagating them into large distances.

The magnetic field of the analytical jet is shown in Figure 7, which is analogous to Figure 6. It was initialized here with a purely toroidal component (see Equation (3)) and acquires a poloidal component as the jet propagates. Still, the ratio between its poloidal and toroidal components is smaller in this jet than in the realistic jet by at least a factor of 2, leading to field lines with a compressed helical shape. From a numerical point of view, this only means that we had to significantly increase the number of integration steps in order to obtain the field lines shown in Figure 7.

4.3. Comparison with Recent Literature

A fundamental difference between this work and most of the existing literature is that the jets we propagate here were launched by the neutron star before its collapse into a black hole. In other works (e.g., Nathanail et al. 2020, 2021; Gottlieb et al. 2022b), the jet component is driven by the black hole.

Additionally, general jet properties were discussed in Murguia-Berthier et al. (2017). They found that a successful jet depends on a jet's head velocity being higher than that of the wind, which occurs in both M20 and here. The authors also argued that, since baryon pollution significantly decreases the
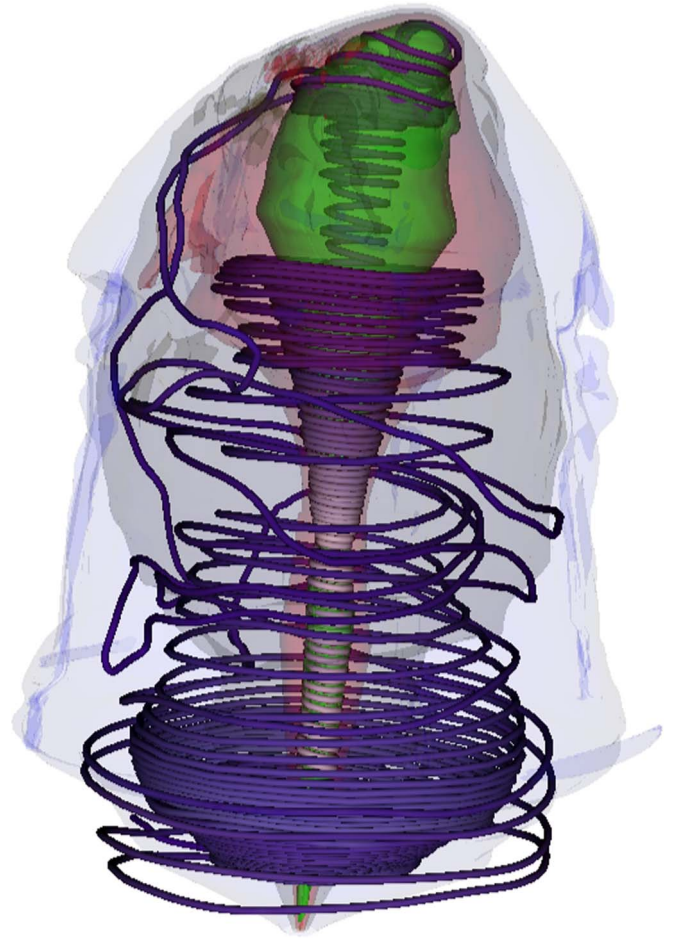

Figure 6. Contour plot of the z-component of the velocity, along with magnetic field lines in the realistic jet, showing the presence of both toroidal and poloidal components. Also shown are contour plots of the jet velocity in the z-direction, here taken at $v_z/c = 0.1$, 0.25, 0.4, and 0.55.

maximum attainable Lorentz factor, a jet would only successfully emerge after the collapse into a black hole.

Our neutron star–launched jet achieves slightly inferior Lorentz factors than those powered by black holes, but the fact that we have a successful jet raises the possibility of the material ejected during the HMNS phase playing a role in sweeping up the immediately surrounding material. Thus, it could pave the way for a strong jet component launched after the collapse into a black hole, especially if this is paired with a longer-lived jet-launching HMNS, whose longer steady-state operation could lead to higher terminal Lorentz factors. Yet in the context of simulations, such quantities are somewhat arbitrary, as they are fundamentally related to density floors and other ad hoc mechanisms added in order to guarantee a stable evolution.

Our assumption (Equation (1)) of a static ejecta is based on the semianalytic model of Lazzati & Perna (2019). To test its validity and implications on the overall structure and motion of the jet (see Hamidani & Ioka 2020, 2023; Gottlieb & Nakar 2022 for the effects of a moving ejecta on the jet), we varied the ejecta velocity in this model between $0.01c$ and $0.3c$ in the neutron star frame. We found that the jet head velocity changes by 8% ($0.65c$ in the slow case versus $0.7c$ in the fast case). Additionally, we found a variation of 6% in the cocoon energy, the fast ejecta being more energetic. We consider these

Figure 7. Same as Figure 6 but for the analytical jet. The ratio between the poloidal and toroidal components in this jet is small, which required us to increase the number of integration steps to obtain the field lines shown here.

adequate if we take into account the uncertainties associated with the model, and as such, we consider our assumption of a static ejecta to be adequate in this context.

5. Conclusions

The main of aim of this work is to show the first steps toward a fully consistent end-to-end description of the BNS merger remnant, as well as the jet launching and propagation. We use a realistic self-consistent jet, extracted from the GRMHD evolution of a highly magnetized BNS merger remnant, to construct a mock long-lived steady-state jet. We employ this steady-state jet as initial data to address the problem of sGRB propagation through a BNS merger static medium. Additionally, as a baseline, we evolve an analytically prescribed jet in the same BNS merger medium. For both cases, we discuss their ability to power sGRBs.

We find that both jets remain collimated and moderately magnetized, achieve moderate velocities of $v \sim 0.6$–$0.7c$ (Lorentz factors of ~ 1.15–1.4), and are surrounded by cocoons with speed $\lesssim 0.5c$. These velocities are close to the maximum attainable velocities of the injected outflows, demonstrating that the acceleration in the ejecta is efficient and that the jet–ejecta interaction is not disruptive. We also find that the numerical, self-consistent jet is slightly more efficient at reaching high velocity, by approximately $\sim 20\%$. This small but significant difference between idealized and realistic

simulations is consistent with Lazzati et al. (2021), who found an $\sim 20\%$ effect when comparing sGRB jet evolution in realistic and idealized ambient materials.

Due to the properties of the injected outflows, we cannot provide a definitive answer to whether jets from magnetars can or cannot power sGRBs, and the main reasons for this conclusion can be associated with numerical, rather than physical, factors. The jets we study here have velocities large enough to contribute to the blue KN component seen in GW170817 and could help preevacuate a channel for the propagation of a subsequent relativistic jet. However, they do not possess velocities large enough to attain a large Lorentz factor. The M20 simulations do show the formation of fast outflows, with their high-resolution case (B15-high) leading to the highest Lorentz factors, $\Gamma \sim 5$. Nonetheless, the simulation we used here, B15-low, is sufficient to describe the large-scale dynamics and propagation of the jet.

Because the flow's maximum speed seems to be limited by numerical constraints (e.g., resolution), there is hope that future general relativistic calculations will provide input of potentially faster jets, either by an increased magnetic field or entropy or thanks to lower baryon contamination. In addition, as seen in the simulation B15-high in M20, resolving the MRI-driven turbulence plays a fundamental role in jet emission, achievable Lorentz factors, and the life span of the remnant, as the HMNS in B15-high lives 7 ms longer than the low-resolution counterpart, an increase of $\sim 20\%$. Furthermore, neutrino effects also play an important role in jet emission in the GRMHD evolution of the remnant, so the inclusion of neutrino pair annihilation may boost the jet's Lorentz factor to the relativistic sGRB regime. If these matters are addressed, it appears reasonable that a simulation where a GRB is powered by a magnetar can be achieved.

ORCID iDs

Gustavo Soares https://orcid.org/0000-0002-6569-5769
Davide Lazzati https://orcid.org/0000-0002-9190-662X

References

Abbott, B. P., Abbott, R., Abbott, T. D., et al. 2017a, ApJL, 848, L12
Abbott, B. P., Abbott, R., Abbott, T. D., et al. 2017b, PhRvL, 119, 161101
Babiuc-Hamilton, M., Brandt, S. R., Diener, P., et al. 2019, The Einstein Toolkit, The "Mayer" Release, ET_2019_10, Zenodo, doi:10.5281/zenodo.3522086
Baumgarte, T. W., Shapiro, S. L., & Shibata, M. 2000, ApJL, 528, L29
Bauswein, A., Goriely, S., & Janka, H. T. 2013, ApJ, 773, 78
Ciolfi, R. 2020, MNRAS, 495, L66
Ciolfi, R., Kastaun, W., Giacomazzo, B., et al. 2017, PhRvD, 95, 063016
Ciolfi, R., Kastaun, W., Kalinani, J. V., & Giacomazzo, B. 2019, PhRvD, 100, 023005

Cook, G. B., Shapiro, S. L., & Teukolsky, S. A. 1992, ApJ, 398, 203
Cook, G. B., Shapiro, S. L., & Teukolsky, S. A. 1994, ApJ, 424, 823
Eichler, D., Livio, M., Piran, T., & Schramm, D. N. 1989, Natur, 340, 126
Fahlman, S., & Fernández, R. 2018, ApJL, 869, L3
Fujibayashi, S., Sekiguchi, Y., Kiuchi, K., & Shibata, M. 2017, ApJ, 846, 114
Gottlieb, O., Bromberg, O., Singh, C. B., & Nakar, E. 2020, MNRAS, 498, 3320
Gottlieb, O., Liska, M., Tchekhovskoy, A., et al. 2022a, ApJL, 933, L9
Gottlieb, O., Moseley, S., Ramirez-Aguilar, T., et al. 2022b, ApJL, 933, L2
Gottlieb, O., & Nakar, E. 2022, MNRAS, 517, 1640
Gottlieb, O., Nakar, E., Piran, T., & Hotokezaka, K. 2018, MNRAS, 479, 588
Hamidani, H., & Ioka, K. 2020, MNRAS, 500, 627
Hamidani, H., & Ioka, K. 2023, MNRAS, 520, 1111
Hotokezaka, K., Kiuchi, K., Kyutoku, K., et al. 2013, PhRvD, 87, 024001
Katz, J. I. 1994, ApJ, 422, 248
Kiuchi, K., Kyutoku, K., Sekiguchi, Y., Shibata, M., & Wada, T. 2014, PhRvD, 90, 041502
Lattimer, J. M., & Douglas Swesty, F. 1991, NuPhA, 535, 331
Lazzati, D., & Perna, R. 2019, ApJ, 881, 89
Lazzati, D., Perna, R., Ciolfi, R., et al. 2021, ApJL, 918, L6
Löffler, F., Faber, J., Bentivegna, E., et al. 2012, CQGra, 29, 115001
Meszaros, P., & Rees, M. J. 1992, MNRAS, 257, 29P
Metzger, B. D. 2019, LRR, 23, 1
Metzger, B. D., Thompson, T. A., & Quataert, E. 2018, ApJ, 856, 101
Mignone, A., Bodo, G., Massaglia, S., et al. 2007, ApJS, 170, 228
Mignone, A., Striani, E., Tavani, M., & Ferrari, A. 2013, MNRAS, 436, 1102
Mignone, A., Ugliano, M., & Bodo, G. 2009, MNRAS, 393, 1141
Mösta, P., Mundim, B. C., Faber, J. A., et al. 2013, CQGra, 31, 015005
Mösta, P., Radice, D., Haas, R., Schnetter, E., & Bernuzzi, S. 2020, ApJL, 901, L37
Murguia-Berthier, A., Ramirez-Ruiz, E., De Colle, F., et al. 2021, ApJ, 908, 152
Murguia-Berthier, A., Ramirez-Ruiz, E., Montes, G., et al. 2017, ApJL, 835, L34
Narayan, R., Paczynski, B., & Piran, T. 1992, ApJL, 395, L83
Nathanail, A., Gill, R., Porth, O., Fromm, C. M., & Rezzolla, L. 2020, MNRAS, 495, 3780
Nathanail, A., Gill, R., Porth, O., Fromm, C. M., & Rezzolla, L. 2021, MNRAS, 502, 1843
O'Connor, E., & Ott, C. D. 2010, CQGra, 27, 114103
Ott, C. D., Abdikamalov, E., O'Connor, E., et al. 2012, PhRvD, 86, 024026
Paczynski, B., & Xu, G. 1994, ApJ, 427, 708
Pavan, A., Ciolfi, R., Kalinani, J. V., & Mignone, A. 2021, MNRAS, 506, 3483
Piran, T., & Sari, R. 1998, in AIP Conf. Proc. 428, Gamma-Ray Bursts, 4th Huntsville Symp., ed. C. A. Meegan, M. D. Preece, & T. M. Koshut, 662
Radice, D., Bernuzzi, S., & Perego, A. 2020, ARNPS, 70, 95
Radice, D., & Rezzolla, L. 2012, A&A, 547, A26
Rees, M. J., & Meszaros, P. 1992, MNRAS, 258, 41P
Rees, M. J., & Meszaros, P. 1994, ApJL, 430, L93
Rezzolla, L., Giacomazzo, B., Baiotti, L., et al. 2011, ApJL, 732, L6
Ruiz, M., Lang, R. N., Paschalidis, V., & Shapiro, S. L. 2016, ApJL, 824, L6
Schnetter, E., Hawley, S. H., & Hawke, I. 2004, CQGra, 21, 1465